

Electrolytic Effect in Solid Oxide Fuel Cells Running on Steam/Methane Mixture

Meng Ni*

Department of Building and Real Estate, The Hong Kong Polytechnic University

Hung Hom, Kowloon, Hong Kong

Abstract

A two-dimensional model is developed to study the performance of a planar solid oxide fuel cell (SOFC) running on steam/methane mixture. The model considers the heat/mass transfer, electrochemical reactions, direct internal reforming of methane (CH_4), and water gas shift reaction in an SOFC. It is found that at an operating potential of 0.8V, the upstream and downstream of SOFC work in electrolysis and fuel cell modes, respectively. At the open-circuit voltage, the electricity generated by the downstream part of SOFC is completely consumed by the upstream through electrolysis, which is contrary to our common understanding that electrochemical reactions cease under the open-circuit conditions. In order to inhibit the electrolytic effect, the SOFC can be operated at a lower potential or use partially pre-reformed CH_4 as the fuel. Increasing the inlet gas velocity from $0.5\text{m}\cdot\text{s}^{-1}$ to $5.0\text{m}\cdot\text{s}^{-1}$ does not reduce the electrolytic effect but decreases the SOFC performance.

Keywords: *solid oxide fuel cells; internal reforming; electrochemistry; porous media; natural gas; electrolysis*

* Corresponding author. Tel. +852 2766 4152; Fax: 852 2764 5131
Email: memni@graduate.hku.hk (M. Ni)

1. Introduction

Solid oxide fuel cells (SOFCs) can directly convert the chemical energy of a fuel into electricity through electrochemical reaction in an efficient and environmentally friendly way. An SOFC usually employs oxygen-ion conducting ceramics as electrolyte, like yttrium-stabilized-zirconia (YSZ) [1-3]. As the electrolyte materials exhibit moderate oxygen ion conductivity at a high temperature, the operating temperature of SOFC is usually high (i.e. 873K-1273K). The high working temperature makes SOFC very suitable for combined heat and power co-generation, as the waste heat from SOFC is of high quality and can be recovered by integrating the SOFC stack with absorption heat pumps or other thermodynamic cycles to achieve a higher overall efficiency [4-6]. Thermodynamic analyses have been reported that the overall efficiency of SOFC/gas turbine system can be higher than 70% [7-9]. In addition, carbon monoxide (CO), a poisonous gas for low temperature fuel cells (i.e. proton exchange membrane fuel cell: PEMFC) [10], does not poison the anode catalyst of SOFC. Instead, CO can be used as a fuel in an SOFC. Thus alternative fuels, like methane, methanol, and ethanol, can be used in SOFCs for power generation [11-21]. The fuel flexibility makes SOFCs more advantageous than hydrogen-fueled fuel cells, as it's still very difficult to produce and store hydrogen effectively and economically. Due to their great prospect for clean power generation, SOFCs have received more and more attention and extensive research works have been conducted in recent years to improve the SOFC efficiency and its long term stability [22-27].

Among a lot of alternative fuels, methane (CH₄) is extensively studied for SOFC as it is the major component in natural gas (about 90%) and one of the major components in biogas [28]. As direct electrochemical oxidation of methane is still difficult in SOFC, methane is usually reformed either externally or internally. External reforming requires additional fuel

processing units for methane steam reforming and water gas shift (WGS) reactions, thus increasing the system's overall cost and complexity [29-35]. For comparison, direct internal reforming (DIR) eliminates the need of an external reformer as the high working temperature enables DIR reaction as well as WGS reaction for H₂ production [36-52]. Thus the SOFC system can be simpler and compact. In addition, part of the thermal energy requirement for DIR reaction can be provided by heat generation in SOFCs, thus a higher overall efficiency can be obtained. However, the endothermic DIR reaction and exothermic WGS reaction complicate the SOFC temperature field and more importantly, both DIR and WGS reactions require steam in the anode, thus diluting the fuel concentration and reducing the SOFC performance. In addition, carbon deposition may occur in a hydrocarbon-fueled SOFC with DIR and WGS, which in turn can deteriorate the SOFC performance considerably [53]. In order to solve the problem of carbon deposition and long term stability, extensive research works have been conducted both experimentally and theoretically. In addition to development of new anode materials, one common way of tackling the carbon deposition problem is to supply sufficient amount of steam in the anode. Based on thermodynamic analysis in the literature, the steam-carbon ratio of no less than 2.0 is usually recommended in order to avoid carbon formation [28,42].

In this short communication, the performance of a planar SOFC running on H₂O/ CH₄ mixture is investigated with a 2D numerical model. It is found that running on H₂O/CH₄ mixture without any pre-reforming, the upstream of the SOFC works in electrolysis mode thus consuming electricity generated in the downstream, at an operating potential of 0.8V. This electrolytic effect in SOFC is due to the non-uniform electrolyte Nernst potential and uniform operating potential along the SOFC channel. This finding is contrary to our common understanding that electrochemical reactions should cease under the open-circuit voltage

conditions. The results of the present study suggest that operating the SOFC at a lower potential, or use partially pre-reformed CH₄ fuel are beneficial to eliminate the electrolytic effect to improve the electric output of CH₄-fueled SOFC.

2. Model Development

In this study, H₂O/ CH₄ mixture with a molar ratio of 2.0 is used in the SOFC anode for power generation via direct internal reforming. The computational domain and working mechanism in a planar SOFC is shown in Figure 1. The computational domain includes the two interconnectors, the fuel gas channel, nickel, yttria-stabilized zirconia (Ni-YSZ) anode, YSZ electrolyte, and YSZ-LSM (lanthanum strontium manganite) cathode, as well as the air gas channel. Typical dimensions of the gas channel and the cell component thickness are used in the modeling study and summarized in Table 1.

During operation, H₂O/ CH₄ mixture and air are supplied to the anode and cathode channels, respectively. In the anode, CH₄ undergoes DIR to produce H₂ and CO (Eq. 1).



Due to a high steam to carbon ratio (2.0 in the present study), WGS reaction occurs in the porous anode as well (Eq. 2).



The H₂ fuel produced from DIR and WGS reaction is transported through the porous anode of the SOFC to the triple-phase-boundary (TPB) at the electrolyte-electrode interface, where H₂ molecules react with oxygen ions (O²⁻) to produce H₂O and electrons (Eq. 3). The electrons produced are transported through external circuit to the cathode to produce useful power. In the cathode, O₂ molecules are transported through the porous cathode to the

electrolyte-cathode interface and react with electrons (coming from anode) to produce oxygen ions (Eq. 4), which are subsequently transported through dense electrolyte to the anode side.



In addition to H_2 , both CO and CH_4 may be electrochemically oxidized in the porous anode. However, since the electrochemical oxidation rates of CO and CH_4 are very small compared with DIR and WGS reactions, electrochemical oxidation of CO and CH_4 can be safely neglected [54-56]. In addition, chemical reaction of CO_2 with CH_4 is assumed to be negligible in the present study.

Based on the working mechanism, a 2D numerical model is developed to capture the coupled transport and chemical/electrochemical reactions in a planar SOFC. The model consists of an electrochemical model, a chemical model and a computational fluid dynamics (CFD) model. The details of the sub-models are described in the subsequent sections.

2.1 Electrochemical Model

The electrochemical model is used to calculate the current density (J) -voltage (V) relationship. It is assumed that the operating potential is constant while the current density varies along the gas flow channel. This is valid as interconnector with high electrical conductivity is placed along the gas channel to collect the current produced in an SOFC. In operation, the J-V relationship can be described by,

$$V = E - \eta_{act,a} - \eta_{act,c} - \eta_{ohmic} \quad (5)$$

$$E = 1.253 - 0.00024516T + \frac{RT}{2F} \ln \left[\frac{P_{\text{H}_2}^I (P_{\text{O}_2}^I)^{0.5}}{P_{\text{H}_2\text{O}}^I} \right] \quad (6)$$

where E is the equilibrium potential (Nernst potential), depending on operating temperature and gas composition; T is the local temperature (K); η_{ohmic} is the ohmic overpotential of the electrolyte (YSZ); $\eta_{act,a}$ and $\eta_{act,c}$ are the activation overpotentials at the anode and cathode, respectively; R is the universal gas constant ($8.3145 \text{ J.mol}^{-1}\text{K}^{-1}$); and F is the Faraday constant (96485 C.mol^{-1}). P^j is the partial pressure at the electrode-electrolyte interface, which means that the concentration overpotentials are included in the Nernst potential (E). The ohmic overpotential can be easily calculated by the Ohm's law. The activation overpotentials are usually calculated with the Butler-Volmer equations. However, as the activation overpotential and current density usually follow a linear relationship according to experimental observations [57], the activation overpotentials are calculated as,

$$\eta_{act} = JR_{act} \quad (7)$$

where R_{act} is the resistivity ($\Omega.m^2$) of the electrode due to electrochemical reaction. Based on the previous study on activation overpotential, the overall resistivity of the anode and cathode of $0.2 \Omega.cm^2$ is used in the present study.

2.2. Chemical model

The chemical model is developed to calculate the rates of DIR and WGS reaction and the resulted heat sink/generation. In the literature, the rates of DIR and WGS reaction can be determined approximately as [58-61],

$$R_{DIR} = (1031.40238 - 1.9844T + (9.55556E - 4)T^2)(1.0E - 8)P_{CH_4}P_{H_2O} - (1.4)(1.0E - 20)P_{CO}(P_{H_2})^3 \quad (8)$$

$$R_{WGS} = (0.02377T - 23.84836)(1.0E - 7)P_{CO}P_{H_2O} - (0.03262T - 33.46016)(1.0E - 7)P_{CO_2}P_{H_2} \quad (9)$$

where R_{DIR} and R_{WGS} are the rates ($\text{mol.m}^{-3}.\text{s}^{-1}$) of DIR and WGS reaction, respectively; and p is the partial pressure (Pa).

The reaction heat for DIR and WGS reaction can be determined by the enthalpy change of the reactions [62]. Assuming linear dependence on temperature, the reaction heat (J.mol^{-1}) for DIR and WGS reaction can be calculated as,

$$H_{DIR} = -(206205.5 + 19.5175T) \quad (10)$$

$$H_{WGS} = 45063 - 10.28T \quad (11)$$

The negative and positive signs in Eqs. (10) and (11) indicate that the DIR and WGS reaction are endothermic and exothermic, respectively.

2.3. Computational fluid dynamics model

The fundamental transport phenomena in an SOFC include fluid flow, heat transfer and mass transfer. In an SOFC, laminar flow conditions are usually applied due to a small Reynolds number. The transport phenomena in SOFCs are governed by the conservation laws for mass, momentum, energy, and species, which are summarized below [63,64]:

$$\frac{\partial(\rho U)}{\partial x} + \frac{\partial(\rho V)}{\partial y} = S_m \quad (12)$$

$$\frac{\partial(\rho U U)}{\partial x} + \frac{\partial(\rho V U)}{\partial y} = -\frac{\partial P}{\partial x} + \frac{\partial}{\partial x} \left(\mu \frac{\partial U}{\partial x} \right) + \frac{\partial}{\partial y} \left(\mu \frac{\partial U}{\partial y} \right) + S_x \quad (13)$$

$$\frac{\partial(\rho U V)}{\partial x} + \frac{\partial(\rho V V)}{\partial y} = -\frac{\partial P}{\partial y} + \frac{\partial}{\partial x} \left(\mu \frac{\partial V}{\partial x} \right) + \frac{\partial}{\partial y} \left(\mu \frac{\partial V}{\partial y} \right) + S_y \quad (14)$$

$$\frac{\partial(\rho c_p U T)}{\partial x} + \frac{\partial(\rho c_p V T)}{\partial y} = \frac{\partial}{\partial x} \left(k \frac{\partial T}{\partial x} \right) + \frac{\partial}{\partial y} \left(k \frac{\partial T}{\partial y} \right) + S_T \quad (15)$$

$$\frac{\partial(\rho U Y_i)}{\partial x} + \frac{\partial(\rho V Y_i)}{\partial y} = \frac{\partial}{\partial x} \left(\rho D_{i,m} \frac{\partial Y_i}{\partial x} \right) + \frac{\partial}{\partial y} \left(\rho D_{i,m} \frac{\partial Y_i}{\partial y} \right) + S_{sp} \quad (16)$$

where U and V are the velocity components in x and y directions; ρ and μ are the gas density and viscosity of the gas mixture respectively, which depends on local temperature and gas composition; k and c_p are the thermal conductivity and heat capacity respectively; Y_i denotes the mass fraction of species i , which can be calculated as,

$$Y_i = X_i \left(\frac{M_i}{M} \right) \quad (17)$$

$$M = \sum_{i=1}^N X_i M_i \quad (18)$$

where X_i and M_i are the molar fraction and molecular weight of species i respectively.

$D_{i,m}^{eff}$ is the effective diffusion coefficient of species i in gas mixture (both anode and cathode) and can be evaluated by Eq. (19)-(21);

$$\frac{1}{D_{i,m}^{eff}} = \frac{\xi}{\varepsilon} \left(\frac{1}{D_{i,m}} + \frac{1}{D_{i,k}} \right) \quad (19)$$

$$D_{i,m} = \frac{1 - X_i}{\sum_{j \neq i} \frac{X_j}{D_{ij}}} \quad (20)$$

$$D_{i,k} = \frac{2r_p}{3} \sqrt{\frac{8RT}{\pi M_i}} \quad (21)$$

where ξ / ε is the ratio of tortuosity to porosity of porous electrodes; and r_p is the radius of pores.

D_{ij} is the binary diffusion coefficient of species i and j , which can be determined as,

$$D_{ij} = \frac{0.0026T^{1.5}}{p \sqrt{M_{i,j}} \sigma_{i,j}^2 \Omega_D} \quad (22)$$

$$M_{ij} = \frac{2}{\frac{1}{M_i} + \frac{1}{M_j}} \quad (23)$$

where $\sigma_{i,j}$ is the mean characteristic length of species i and j ; Ω_D is a dimensionless diffusion collision integral, which can be calculated as,

$$\sigma_{i,j} = \frac{\sigma_i + \sigma_j}{2} \quad (24)$$

$$\Omega_D = \frac{1.06036}{\tau^{0.1561}} + \frac{0.193}{\exp(0.47635\tau)} + \frac{1.03587}{\exp(1.52996\tau)} + \frac{1.76474}{3.89411\tau} \quad (25)$$

$$\tau = \frac{k_b T}{\varepsilon_{i,j}} \quad (26)$$

where $k_b = 1.38066 \times 10^{-23}$ (J.K⁻¹) is the Boltzmann's constant. The values of σ_i and $\varepsilon_{i,j}$ can be used in the present study are summarized in Table 2 [65].

In the porous electrodes, effective heat conductivity and heat capacity are used [66],

$$k = \varepsilon k_f + (1 - \varepsilon) k_s \quad (27)$$

$$c_p = \varepsilon c_{p,f} + (1 - \varepsilon) c_{p,s} \quad (28)$$

where k_f and k_s are the heat conductivity (W.m⁻¹.K⁻¹) of the fluid and solid, respectively; $c_{p,f}$ and $c_{p,s}$ are the heat capacity (J.kg⁻¹.K⁻¹) of the fluid and solid, respectively.

The source term S in continuity equation (Eq. 12) represents the mass change due to electrochemical reactions. As electrochemical reactions are assumed to occur only at the electrode-electrolyte interface, the source term is non-zero at the electrode-electrolyte interface and zero in other regions. At the anode-electrolyte interface, the source term for continuity equation can be written as [66],

$$S_m = \left(\frac{JM_{H_2O}}{2F} - \frac{JM_{H_2}}{2F} \right) \frac{A_{act}}{V_c} = \frac{JM_{H_2O}}{2F\Delta y} - \frac{JM_{H_2}}{2F\Delta y} \quad (29)$$

where A_{act} is the active area for electrochemical reaction at the anode-electrolyte interface and V_c is the size of control volume. Δy is the width of the control volume in y direction at the anode-electrolyte interface. At the cathode-electrolyte interface, this source term is calculated as,

$$S_m = -\frac{JM_{O_2}}{4F\Delta y} \quad (30)$$

where the negative sign above means oxygen is electrochemically consumed.

The Darcy's law is used as source terms in momentum equations (Eqs. 13 and 14) so that the momentum equations are valid for both the gas channels and the porous electrodes [64];

$$S_x = \frac{\mu U}{B_g} \quad (31)$$

$$S_y = \frac{\mu V}{B_g} \quad (32)$$

The source term ($W.m^{-3}$) in energy equation (Eq. 11) includes: (1) heat generation due to electrochemical entropy change and irreversible overpotentials; (2) heat energy demand for DIR (Eq. 1); and heat generation due to WGS reaction (Eq. 2). In the porous anode, both DIR and WGS contributes to the source term,

$$S_T = R_{DIR}H_{DIR} + R_{WGS}H_{WGS} \quad (33)$$

In the dense electrolyte, the source term includes the irreversible loss through entropy change and activation losses via electrochemical reaction (at the electrode-electrolyte interface), as well as ohmic overpotential of the electrolyte. These losses are assumed to evenly distributed in the electrolyte and thus the source term can be written as,

$$S_T = -\frac{JT\Delta S}{2FL} + \frac{J\eta_t}{L} \quad (34)$$

where L is the thickness of electrolyte; ΔS is the entropy change of the electrochemical reaction ($\text{J.K}^{-1}.\text{mol}^{-1}$) and can be calculated as,

$$\Delta S = S_{H_2O} - 0.5S_{O_2} - S_{H_2} \quad (35)$$

where S_{H_2O} , S_{O_2} and S_{H_2} are entropy of H_2O , O_2 , and H_2 , respectively, which can be found in reference [62]. The negative ΔS indicates that heat is released from the electrochemical reaction.

η_t (V) is the total overpotential losses, which can be calculated as,

$$\eta_t = V - E \quad (36)$$

The source terms (S_{sp}) in species equations (Eq. 16) can be calculated in the way similar to the source term for continuity equation (Eq. 12). However, in the anode, the DIR and WGS reaction should be included.

3. Numerical Methodology

The governing equations are solved with the finite volume method [67]. The boundary conditions and the detailed calculation procedures can be found in the previous publication [64]. The electrochemical model and the chemical model are linked with the CFD model through the source terms in Eqs. (12)-(16). In the iteration, the electrochemical model and the chemical model are solved to calculate the current density and chemical reaction rates, which are used to determine the source terms for the CFD model. Subsequently, the CFD model is solved to update the temperature, gas composition, fluid velocity in SOFC, which are used to solve the

electrochemical model and the chemical model. Computation is repeated until convergence is obtained. The in-house CFD code is written in FORTRAN.

4. Results and Discussion

The electrochemical model, chemical model and the CFD model have been validated respectively in the previous publications, by comparing the modeling results with data from the literature [61, 64]. Numerical simulations have been carried out to ensure grid independence of the results. The dimensions and typical structural/operating parameters used are summarized in Table 1. As mentioned in the introduction, a carbon-steam ratio of 2.0 is used in the present study in order to avoid carbon deposition. In terms of molar fraction, 0.667 and 0.333 are used for H₂O and CH₄ at the anode inlet.

4.1. Electrolytic effect in SOFC running on H₂O/ CH₄ mixture

One significant finding of the present study is that the current density of SOFC running on H₂O/CH₄ mixture increases sharply from a **negative value** near the SOFC inlet to be on the order of 1000 A.m⁻² in the downstream of SOFC, at an operating potential of 0.8V (Fig. 2a). The negative current density near the inlet indicates that the upstream of the SOFC works in the **electrolysis** mode. The positive current density in the downstream of SOFC indicates that the downstream of SOFC works in fuel cell mode and provides the electrical energy needed for H₂O electrolysis near the inlet, as the electrical conductivity of the current collector (interconnector) placed on the entire SOFC channel is very high. As can be seen from Fig. 2b, the electrolyte Nernst potential increases from below 0.8V near the inlet to be slightly higher than 0.9 at the outlet of the SOFC. The low Nernst potential is mainly because the partial pressure ratio of H₂

to H₂O is low near the inlet (Eq. 6). The non-uniform local Nernst potential and the uniform operating potential cause the electrolytic effect found in the present study, since the operating potential (0.8V) is higher than the local Nernst potential in the upstream but lower than the local Nernst potential in the downstream of SOFC running on H₂O/CH₄ mixture. This finding for SOFC has not been reported before because almost all modeling studies on CH₄ fueled SOFC assumes that part of CH₄ is externally reformed (typically about 30% pre-reformed) before feeding to the anode of SOFC (i.e. [37]-[41]). The present study also indicates that at open-circuit voltage condition, the electricity produced in the downstream of SOFC is exactly used up through electrolysis in the upstream of SOFC. It is contrary to conventional understanding that electrochemical reactions should cease at open-circuit voltage. However, this finding is similar to the experimental observations in Prof. Zhao's work on direct methanol fuel cells (DMFCs) [68-71]. In their works, electrolytic hydrogen evolution was observed in a DMFC at open-circuit voltage [68-71]. The reason is that part of the DMFC works in fuel cell mode, producing electricity, while part of DMFC works in electrolytic mode, consuming electricity and producing H₂ gas, which experimentally supports the finding of the present study.

In order to better understand the electrolytic effect and the working mechanisms, the distributions of DIR and WGS reaction as well as gas composition in the SOFC are studied. In the porous anode, the rate of DIR decreases considerably from about 388mol.m⁻³.s⁻¹ near the inlet to be less than 100mol.m⁻³.s⁻¹ in about 7mm downstream from the inlet (Fig. 3a). In the further downstream, the rate of DIR does not vary much along the channel. For comparison, a locally high rate (over 80mol.m⁻³.s⁻¹) of WGS reaction is observed in the porous anode, and in most of the anode the rate of WGS reaction is about 30-50 mol.m⁻³.s⁻¹ (Fig. 3b). The calculated reaction rates are on the same order but a little higher than the data by Lehnert et al. [58]. The

higher reaction rate for DIR and WGS may be caused by a higher temperature and a higher H₂O molar fraction used in the present study.

Due to the electrolytic effect near the inlet, the DIR and WGS reaction, H₂ molar fraction increases considerably from 0.0 at the inlet to be higher than 0.23, despite of electrochemical reduction of H₂ in most part of the SOFC (Fig. 4a). The molar fraction of CH₄ decreases along the SOFC channel due to DIR, as shown in Fig. 4b. The decrease in SOFC temperature along the channel indicates that the heat sink due to endothermic internal reforming of CH₄ is higher than heat generation due to irreversible losses and the WGS reaction (Fig. 5). The temperature difference between the inlet and outlet is more than 73K in the present simulation. The temperature distribution in the present study is different from an SOFC running on partially reformed CH₄ gas mixture, i.e. work done by Aguiar et al. [39]. In an SOFC fueled with a gas mixture of CH₄, H₂O, H₂, CO, CO₂ (partially pre-reformed), the temperature decreases near the inlet, reaches the minimum, and increases in the downstream [39]. This means that if CH₄ is partially (i.e. 30%) pre-reformed, the heat generation due to WGS reaction and electrochemical reaction can exceed the heat demand for DIR in the downstream of SOFC.

4.2. Effect of operating potential

Since the electrolytic effect in an SOFC running on H₂O/CH₄ mixture is caused by the higher operating potential than the local Nernst potential, this effect may be eliminated by operating the SOFC at a lower potential. As shown in Fig. 6a and 6b, the local current density increases from a positive value along the SOFC channel, indicating that the electrolytic effect is removed since the operating potential (0.4V) is lower than the local Nernst potential. As the current density of SOFC at an operating potential of 0.4V (Fig. 2a) is significantly higher than at

0.8V (Fig. 6a), heat generation from electrochemical reactions increases, which results in a higher temperature in the downstream of SOFC at an operating potential of 0.4V. As can be seen from Fig. 7, the temperature at the outlet of SOFC is increased from 1100K at 0.8V to 1133K at 0.4V. As a result, the rates of DIR and WGS reaction in the downstream of the SOFC are slightly increased when the operating potential is decreased from 0.8V to 0.4V (Fig. 8a, 8b)

4.3. Effect of inlet gas velocity

As another important operating parameter, the inlet gas velocity is varied to examine its effect on SOFC performance. It is found that an increase in inlet gas velocity from $0.5\text{m}\cdot\text{s}^{-1}$ to $5.0\text{m}\cdot\text{s}^{-1}$ has negligible effect on the current density and Nernst potential near the inlet but significantly decrease both the current density and Nernst potential in the downstream of the SOFC (Fig. 9a, 9b). This phenomenon is attributed to the fact that the gas composition has smaller variation at a higher inlet gas velocity than at a smaller inlet gas velocity, as more gas is supplied to the SOFC. As can be seen from Fig. 10a, the H_2 molar fraction increases considerably from 0.0 (inlet of SOFC) to about 0.3 (outlet of SOFC) at an inlet gas velocity of $0.5\text{m}\cdot\text{s}^{-1}$. For comparison, the H_2 molar fraction only increases to about 0.1 at the outlet of SOFC at an inlet gas velocity of $5.0\text{m}\cdot\text{s}^{-1}$ (Fig. 10b). Similarly, the H_2O molar fraction in the downstream of SOFC is found higher at an inlet gas velocity of $5.0\text{m}\cdot\text{s}^{-1}$ than at an inlet velocity of $0.5\text{m}\cdot\text{s}^{-1}$ (Fig. 11). The higher ratio of $\text{H}_2/\text{H}_2\text{O}$ (molar fraction) at a higher velocity leads to a higher electrolyte Nernst potential as well as a higher current density, as shown in Fig. 9. In addition, the smaller variation in gas composition at a higher inlet gas velocity results in higher DIR (Fig. 12) and WGS reaction (Fig. 13) in the downstream than at a smaller inlet gas velocity, since more reactants are supplied at a higher velocity. For example, at an inlet gas velocity of

5.0m.s^{-1} , the rates of DIR and WGS reaction near the outlet of SOFC are about $100\text{mol.m}^{-3}.\text{s}^{-1}$ and $40\text{mol.m}^{-3}.\text{s}^{-1}$, respectively (Figs. 12b, 13b). At a smaller inlet gas velocity (0.5m.s^{-1}), these two reaction rates near the SOFC outlet are about $50\text{mol.m}^{-3}.\text{s}^{-1}$ and $20\text{mol.m}^{-3}.\text{s}^{-1}$, respectively (Figs. 12a, 13a).

5. Conclusion

A numerical model is developed to study the performance of SOFC running on $\text{H}_2\text{O}/\text{CH}_4$ mixture considering DIR and WGS reaction in the porous anode. It is found that at an operating potential of 0.8V , or at the open-circuit voltage, the upstream of SOFC works in electrolysis mode while the downstream of SOFC works in fuel cell mode. The electrolytic effect in SOFC is caused by the non-uniform local Nernst potential and uniform operating potential along the SOFC channels. At the open-circuit voltage, both H_2O electrolysis and fuel cell reactions take place in the SOFC running on $\text{H}_2\text{O}/\text{CH}_4$ mixture and the electricity generated from the fuel cell part is exactly used up by the electrolysis part. This finding is contrary to conventional understanding that electrochemical reactions should cease at open-circuit voltages.

The electrolytic effect in the SOFC can be eliminated by operating the SOFC at a sufficiently low potential – lower than the local Nernst potential. At a lower operating potential, the current density is considerably increased, which in turn results in higher heat generation through electrochemical reaction and thus a higher temperature in the downstream of SOFC. An increase in inlet gas velocity from 0.5m.s^{-1} to 5.0m.s^{-1} does not contribute to the reduction of electrolytic effect. Instead, the electrical output of SOFC is reduced at a higher inlet gas velocity, as both the average current density and Nernst potential are decreased.

This study provides better understanding of the CH₄-fueled SOFC with internal reforming and indicates that partial pre-reforming of CH₄ is beneficial for SOFC considering the electrolytic effect.

Acknowledgments

This research was supported by a grant from the Start-up Research Fund for newly recruited Assistant Professors (Project No. 1-ZV6M), The Hong Kong Polytechnic University, Hong Kong.

Nomenclature

c_p	Heat capacity ($\text{J.kg}^{-1}.\text{K}^{-1}$)
d_a	Thickness of anode (μm)
d_c	Thickness of cathode (μm)
$D_{i,m}^{eff}$	Effective diffusion coefficient of species i in gas mixture ($\text{cm}^2.\text{s}^{-1}$)
$D_{i,k}$	Knudsen diffusion coefficient of i ($\text{cm}^2.\text{s}^{-1}$)
$D_{i,j}$	Binary diffusion coefficient of i and j ($\text{cm}^2.\text{s}^{-1}$)
E	Equilibrium potential (V)
E_0	Reversible potential at standard condition (V)
F	Faraday constant ($9.6485 \times 10^4 \text{ C.mol}^{-1}$)
H_{DIR}	Heat demand for direct internal reforming of methane (J.mol^{-1})
H_{WGS}	Heat generation from water gas shift reaction (J.mol^{-1})
J	Current density (A.m^{-2})
k	Thermal conductivity ($\text{W.m}^{-1}.\text{K}^{-1}$)
M_i	Molecular weight of species i (kg.mol^{-1})
P	Operating pressure (bar)
P_i^I	Partial pressure (bar) of species i at electrode-electrolyte interface
R_{act}	Resistivity due to electrochemical reaction ($\Omega.\text{m}^2$)
R_{DIR}	Reaction rate of direct internal reforming of methane ($\text{mol.m}^{-3}.\text{s}^{-1}$)
R_{WGS}	Rate of water gas shift reaction ($\text{mol.m}^{-3}.\text{s}^{-1}$)
r_p	Mean pore radius of electrode (μm)

R	Universal gas constant ($8.3145 \text{ J.mol}^{-1}.\text{K}^{-1}$)
S_i	Entropy of species i (i represents H_2O , H_2 , and O_2)
S_m	Source term in continuity equation ($\text{kg.m}^{-3}.\text{s}^{-1}$)
S_x, S_y	Source terms in momentum equations ($\text{kg.m}^{-2}.\text{s}^{-2}$)
S_T	Source terms in energy equations (W.m^{-3})
S_{sp}	Source terms in species equations ($\text{kg.m}^{-3}.\text{s}^{-1}$)
T	Operating temperature (K)
U	Velocity in x direction (m.s^{-1})
U_{in}	Gas velocity at the SOFC inlet (m.s^{-1})
V	SOFC operating potential (V); Velocity in y direction (m.s^{-1})
X	Molar fraction of species i
Y	Mass fraction of species i
ε	Electrode porosity
ξ	Electrode tortuosity
$\sigma_{i,j}$	Mean characteristic length of species i and j
Ω_D	Dimensionless diffusion collision integral
ρ	Density of the gas mixture (kg.m^{-3})
μ	Viscosity of gas mixture ($\text{kg.m}^{-1}.\text{s}^{-1}$)
$\eta_{act,a}$	Activation overpotential at anode (V)
$\eta_{act,c}$	Activation overpotential at cathode (V)
η_{ohmic}	Ohmic overpotential of the electrolyte (V)

References

- [1] S.C. Singhal, K. Kendall, High Temperature Solid Oxide Fuel Cells – Fundamentals, Design and Applications, Elsevier, New York, 2003.
- [2] N. Sammes, Fuel Cell Technology: Reaching Towards Commercialization, Springer, London, 2006.
- [3] K. Huang, J.B. Goodenough, Solid Oxide Fuel Cell Technology: Principles, Performance and Operations, Cambridge [England], Woodhead Publishing, 2009.
- [4] X.W. Zhang, S.H. Chan, G.J. Li, H.K. Ho, J. Li, Z.P. Feng, A review of integration strategies for solid oxide fuel cells, *J. Power Sources*, **195** (2010): 685-702.
- [5] A.D. Hawkes, P. Aguiar, B. Croxford, M.A. Leach, C.S. Adjiman, N.P. Brandon, Solid oxide fuel cell micro combined heat and power system operating strategy: options for provision of residential space and water heating, *J. Power Sources*, **164** (2007): 260-271.
- [6] C. Bao, Y.X. Shi, E. Croiset, C. Li, N.S. Cai, A multi-level simulation platform of natural gas internal reforming solid oxide fuel cell-gas turbine hybrid generation system: part 1. solid oxide fuel cell model library, *J. Power Sources*, **195** (2010): 4871-4892.
- [7] Y.F. Yi, A.D. Rao, J. Brouwer, G.S. Samuelsen, Analysis and optimization of a solid oxide fuel cell and intercooled gas turbine (SOFC-ICGT) hybrid cycle, *J. Power Sources*, **132** (2004): 77-85.
- [8] F. Calise, M.D. d'Accadia, A. Palombo, L. Vanoli, Simulation and exergy analysis of a hybrid solid oxide fuel cell (SOFC)-gas turbine system, *Energy*, **31** (2006): 3278-3299.
- [9] C. Stiller, B. Thorud, S. Seljebo, O. Mathisen, H. Karoliussen, O. Bolland, Finite-volume modeling and hybrid-cycle performance of planar and tubular solid oxide fuel cells, *J. Power Sources*, **141** (2005): 227- 240.
- [10] T.S. Zhao, K.D. Kreuer, T. Nguyen, Advances in Fuel Cells, Elsevier, 2007, ISBN-13: 978-0-08-045394-1.
- [11] K. Eguchi, H. Kojo, T. Takeguchi, R. Kikuchi, K. Sasaki, Fuel flexibility in power generation by solid oxide fuel cells, *Solid State Ionics*, **152-153** (2002): 411-416.
- [12] Y.F. Yi, A.D. Rao, J. Brouwer, G.S. Samuelsen, Fuel flexibility study of an integrated 25kW SOFC reformer system, *J. Power Sources*, **144** (2005): 67-76.
- [13] M.M. Hussain, X. Li, I. Dincer, A general electrolyte-electrode-assembly model for the performance characteristics of planar anode-supported solid oxide fuel cells, *J. Power Sources*, **189** (2009): 916-928.
- [14] F.P. Nagel, T.J. Schildhauer, S.M.A. Biollaz, A. Wokaun, Performance comparison of planar, tubular and Delta8 solid oxide fuel cells using a generalized finite volume model, *J. Power Sources*, **184** (2008): 143-164.
- [15] T. Hibino, A. Hashimoto, T. Inoue, J. Tokuno, S. Yoshida, M. Sano, A low-operating-temperature solid oxide fuel cell in hydrocarbon-air mixtures, *Science*, **288** (2000): 2031-2033.
- [16] Z.L. Zhan, S.A. Barnett, An octane-fueled solid oxide fuel cell, *Science*, **308** (2005): 844-847.
- [17] P. Piroonlerkgul, W. Wiyaratn, A. Soottitantawat, W. Kiatkittipong, A. Arpornwichanop, N. Laosiripojana, S. Assabumrungrat, Operation viability and performance of solid oxide fuel cell fueled by different feeds, *Chemical Engineering Journal*, **155** (2009): 411-418.
- [18] A. Wojcik, H. Middleton, I. Damopoulos, J.V. Herle, Ammonia as a fuel in solid oxide fuel cells, *J. Power Sources*, **118** (2003): 342-348.

- [19] S. Douvartzides, F. Coutelieris, P. Tsiakaras, Exergy analysis of a solid oxide fuel cell power plant fed by either ethanol or methane, *J. Power Sources*, **131** (2004): 224-230.
- [20] M.F. Liu, R.R. Peng, D.H. Dong, J.F. Gao, X.Q. Liu, G.Y. Meng, Direct liquid methanol-fueled solid oxide fuel cell, *J. Power Sources*, **185** (2008): 188-192.
- [21] G.K. Gupta, A.M. Dean, K. Ahn, R.J. Gorte, Comparison of conversion and deposit formation of ethanol and butane under SOFC conditions, *J. Power Sources*, **158** (2006): 497-503.
- [22] L. Liu, G.Y. Kim, A. Chandra, Modeling of thermal stresses and lifetime prediction of planar solid oxide fuel cell under thermal cycling conditions, *J. Power Sources*, **195** (2010): 2310-2318.
- [23] A. Nakajo, Z. Wuillemin, J. Van. Herle, D. Favrat, Simulation of thermal stresses in anode-supported solid oxide stacks, Part II: loss of gas tightness, electrical contact and thermal buckling, *J. Power Sources*, **193** (2009): 216-226.
- [24] Y.X. Zhang, C.R. Xia, A durability model for solid oxide fuel cell electrodes in thermal cycle processes, *J. Power Sources*, **195** (2010): 6611-6618.
- [25] S.X. Liu, W. Kong, Z.J. Lin, Three-dimensional modeling of planar solid oxide fuels and the rib design optimization, *J. Power Sources*, **194** (2009): 854-863.
- [26] K.P. Recknagle, E.M. Ryan, B.J. Koepfel, L.A. Mahoney, M.A. Khaleel, Modeling of electrochemistry and steam-methane reforming performance for simulating pressurized solid oxide fuel cell stack, *J. Power Sources*, **195** (2010): 6637-6644.
- [27] W.N. Liu, X. Sun, M.A. Khaleel, J.M. Qu, Global failure criteria for positive/electrolyte/negative structure of planar solid oxide fuel cell, *J. Power Sources*, **192** (2009): 486-493.
- [28] D. Mogensen, J.D. Grunwaldt, P.V. Hendriksen, K. Dam-Johansen, J.U. Nielsen, Internal steam reforming in solid oxide fuel cells: status and opportunities of kinetic studies and their impact on modeling, *J. Power Sources*, 2010, in press.
- [29] S. Lee, J. Bae, S. Lim, J. Park, Improved configuration of supported nickel catalysts in a steam reformer for effective hydrogen production from methane, *J. Power Sources*, **180** (2008): 506-515.
- [30] T.A. Adams II, P.I. Barton, High-efficiency power production from natural gas with carbon capture, *J. Power Sources*, **195** (2010): 1971-1983.
- [31] R. Peters, E. Riensche, P. Cremer, Pre-reforming of natural gas in solid oxide fuel-cell systems, *J. Power Sources*, **86** (2000): 432-441.
- [32] C. Finnerty, G.A. Tompsett, K. Kendall, R.M. Ormerod, SOFC system with integrated catalytic fuel processing, *J. Power Sources*, **86** (2000): 459-463.
- [33] S.H. Chan, O.L. Ding, Simulation of a solid oxide fuel cell power system fed by methane, *Int. J. Hydrogen Energy*, **30** (2005): 167-179.
- [34] R.T. Leah, N.P. Brandon, P. Aguiar, Modelling of cells, stacks and systems based around metal-supported planar IT-SOFC cells with CGO electrolytes operating at 500-600°C, *J. Power Sources*, **145** (2005): 336-352.
- [35] F. Mueller, F. Jabbari, R. Gaynor, J. Brouwer, Novel solid oxide fuel cell system controller for rapid load following, *J. Power Sources*, **172** (2007): 308-323.
- [36] E. Achenbach and E. Riensche, Methane/steam reforming kinetics for solid oxide fuel cells, *J. Power Sources*, **52** (1994): 283-288.
- [37] E. Achenbach, Three-dimensional and time-dependent simulation of a planar solid oxide fuel cell stack, *J. Power Sources*, **49** (1994): 333-348.
- [38] H. Zhu and R.J. Kee, A general mathematical model for analyzing the performance of fuel-cell membrane-electrode assemblies, *J. Power Sources*, **117** (2003): 61-74.

- [39] P. Aguiar, C.S. Adjiman, N.P. Brandon, Anode-supported intermediate temperature direct internal reforming solid oxide fuel cell. I: model-based steady-state performance, *J. Power Sources*, **138** (2004): 120-136.
- [40] H. Yakabe, T. Ogiwarw, M. Hishinuma and I. Yasuda, 3-D model calculation for planar SOFC, *J. Power Sources*, **102** (2001): 144–154.
- [41] P. Iora, P. Aguiar, C.S. Adjiman, N.P. Brandon, Comparison of two IT DIR-SOFC models: impact of variable thermodynamic, physical, and flow properties, steady-state and dynamic analysis, *Chemical Engineering Science*, **60** (2005): 2963-2975.
- [42] J. Brouwer, Support for the high efficiency, carbon separation and internal reforming capabilities of solid oxide fuel cell systems, *J. Power Sources*, **195** (2010): 5150-5151.
- [43] C.O. Colpan, F.H. Hamdullahpur, I. Dincer, Heat-up and start-up modeling of direct internal reforming solid oxide fuel cells, *J. Power Sources*, **195** (2010): 3579-3589.
- [44] A. Arpornwichanop, Y. Patcharavorachot, S. Assabumrungrat, Analysis of a proton-conducting SOFC with direct internal reforming, *Chemical Engineering Science*, **65** (2010): 581-589.
- [45] J.M. Klein, M. Henault, C. Roux, Y. Bultel, S. Georges, Direct methane solid oxide fuel cell working by gradual internal steam reforming: analysis of operation, *J. Power Sources*, **193** (2009): 331-337.
- [46] Y.W. Kang, J. Li, G.Y. Cao, H.Y. Tu, J. Li, J. Yang, A reduced 1D dynamic model of a planar direct internal reforming solid oxide fuel cell for system research, *J. Power Sources*, **188** (2009): 170-176.
- [47] T.X. Ho, P. Kosinski, A.C. Hoffmann, A. Vik, Numerical analysis of a planar anode-supported SOFC with composite electrodes, *Int. J. Hydrogen Energy*, **34** (2009): 3488-3499.
- [48] W.G. Bessler, S. Gewies, M. Vogler, A new framework for physically based modeling of solid oxide fuel cells, *Electrochimica Acta*, **53** (2007): 1782-1800.
- [49] V.M. Janardhanan, O. Deutschmann, CFD analysis of a solid oxide fuel cell with internal reforming: coupled interactions of transport, heterogeneous catalysis and electrochemical processes, *J. Power Sources*, **162** (2006): 1192-1202.
- [50] H.Y. Zhu, R.J. Kee, Modeling Electrochemical Impedance Spectra in SOFC Button Cells with Internal Methane Reforming, *J. Electrochem. Soc.*, **153** (2006): A1765-A1772.
- [51] W.G. Bessler, S. Gewies, M. Vogler, A new approach for elementary-kinetic modeling of internal-reforming SOFCs, *ECS Transactions*, **7** (2007): 1801-1810.
- [52] K. Nikooyeh, A.A. Jeje, J.M. Hill, 3D modeling of anode-supported planar SOFC with internal reforming of methane, *J. Power Sources*, **171** (2007): 601-609.
- [53] T. Matsui, R. Kishida, J.Y. Kim, H. Muroyama, K. Eguchi, Performance deterioration of Ni-YSZ anode induced by electrochemically generated steam in solid oxide fuel cells, *J. Electrochem. Soc.*, **157** (2010): B776-B781.
- [54] Y. Matsuzaki, I. Yasuda, Electrochemical Oxidation of H₂ and CO in a H₂-H₂O-CO-CO₂ System at the Interface of a Ni-YSZ Cermet Electrode and YSZ Electrolyte, *J. Electrochem. Soc.*, **147** (2000): 1630–1635.
- [55] V.M. Janardhanan and O. Deutschmann, Numerical study of mass and heat transport in solid-oxide fuel cells running on humidified methane, *Chemical Engineering Science* **62** (2007) 5473–5486.
- [56] M. Ni, D.Y.C. Leung, M.K.H. Leung, Importance of pressure gradient in solid oxide fuel cell electrodes for modeling study, *J. Power Sources* **183** (2008) 668-673.

- [57] Personal communication with Dr. M. S. Sohal from Idaho National Laboratory, at ASME 2010 8th International Fuel Cell Science, Engineering & Technology Conference, June 14-16, 2010, Brooklyn, New York, USA.
- [58] W. Lehnert, J. Meusinger and F. Thom, Modelling of gas transport phenomena in SOFC anodes, *J. Power Sources* **87** (2000) 57–63.
- [59] P. Ivanov, Thermodynamic modeling of the power plant based on the SOFC with internal steam reforming of methane, *Electrochim Acta* **52** (2007) 3921–3928.
- [60] E.S. Greene, W.K.S. Chiu and M.G. Medeiros, Mass transfer in graded microstructure solid oxide fuel cell electrodes, *J Power Sources* **161** (2006) 225–232.
- [61] M. Ni, D.Y.C. Leung, M.K.H. Leung, Electrochemical modeling and parametric study of methane fed solid oxide fuel cells, *Energy Conversion and Management* **50** (2009) 268-278.
- [62] M.W. Chase, NIST-JANAF thermochemical tables (4th ed.), American Chemical Society, American Institute of Physics for the National Institute of Standards and Technology, 1998.
- [63] C.Y. Wang, Fundamental models for fuel cell engineering, *Chem Rev* **104** (2004) 4727–4765.
- [64] M. Ni, Computational fluid dynamics modeling of a solid oxide electrolyzer cell for hydrogen production, *Int. J. Hydrogen Energy* **34** (2009) 7795-7806.
- [65] R.C. Reid, J.M. Prausnitz and B.E. Poling, The properties of gases & liquids (4th ed.), McGraw-Hill Book Company, New York (1987).
- [66] J.L. Yuan, Y. Huang, B. Sundén and W.G. Wang, CFD Approach to Analyze Parameter Effects on Chemical-Reacting Transport Phenomena in SOFC Anodes, *Heat and Mass Transfer* **45** (2009) 471-484.
- [67] S.V. Patankar, Numerical heat transfer and fluid flow, McGraw-Hill, New York (1980).
- [68] Q. Ye, T.S. Zhao, H. Yang, J. Prabhuram, Electrochemical reaction in a DMFC under open-circuit conditions, *Electrochemical and Solid-State Letters* **8** (2005) A52-A54.
- [69] Q. Ye, T.S. Zhao, Electrolytic hydrogen evolution in DMFCs induced by oxygen interruptions and its effect on cell performance, *Electrochemical and Solid-State Letters* **8** (2005) A211-A214.
- [70] Q. Ye, T.S. Zhao, Abrupt decline in the open-circuit voltage of direct methanol fuel cells at critical oxygen feed rate, *J. Electrochemical Society* **152** (2005) A2238-A2245.
- [71] Q. Ye, T.S. Zhao, J.G. Liu, Effect of transient hydrogen evolution/oxygen reactions on the OCV of direct methanol fuel cells, *Electrochemical and Solid-State Letters* **8** (2005) A549-A553.

List of Tables

1. Parameters used in simulation
2. Parameters used in calculating the effective diffusion coefficients [65]

List of Figures

1. Computational domain of a planar SOFC running on H₂O/CH₄ mixture
2. Electrolytic effect in SOFC running on H₂O/CH₄ mixture at an operating potential of 0.8V – (a) Distribution of current density; (b) Distribution of electrolyte Nernst potential;
3. Distribution of chemical reaction rates in SOFC at an operating potential of 0.8V – (a) Direct internal reforming of CH₄; (b) Water gas shift reaction;
4. Distribution of gas composition in SOFC – (a) H₂ molar fraction; (b) H₂O molar fraction; (c) CH₄ molar fraction;
5. Distribution of temperature in SOFC running on H₂O/CH₄ mixture;
6. Electrochemical performance of SOFC at an operating potential of 0.4V – (a) Distribution of current density; (b) Distribution of electrolyte Nernst potential;
7. Distribution of temperature in SOFC running on H₂O/CH₄ mixture at an operating potential of 0.4V;
8. Distribution of chemical reaction rates in SOFC at an operating potential of 0.4V – (a) Direct internal reforming of CH₄; (b) Water gas shift reaction;
9. Comparison of SOFC electrochemical performance at inlet gas velocity of 0.5m.s⁻¹ and 5.0m.s⁻¹ – (a) Distribution of current density; (b) Distribution of electrolyte Nernst potential;
10. Distribution of H₂ molar fraction in SOFC running on H₂O/CH₄ mixture – (a) Inlet gas velocity: 0.5m.s⁻¹; (b) Inlet gas velocity: 5.0m.s⁻¹;
11. Distribution of H₂O molar fraction in SOFC running on H₂O/CH₄ mixture – (a) Inlet gas velocity: 0.5m.s⁻¹; (b) Inlet gas velocity: 5.0m.s⁻¹;
12. Distribution of direct internal reforming rate SOFC running on H₂O/CH₄ mixture – (a) Inlet gas velocity: 0.5m.s⁻¹; (b) Inlet gas velocity: 5.0m.s⁻¹;
13. Distribution of water gas shift reaction rate in SOFC running on H₂O/CH₄ mixture – (a) Inlet gas velocity: 0.5m.s⁻¹; (b) Inlet gas velocity: 5.0m.s⁻¹;

Table 1. Parameters used in simulation

Parameter	Value
Operating temperature, T (K)	1173
Operating pressure, P (bar)	1.0
Electrode porosity, ε	0.4
Electrode tortuosity, ξ	3.0
Average pore radius, r_p (μm)	0.5
Anode-supported electrolyte:	
Anode thickness d_a (μm)	500
Electrolyte thickness, L (μm)	100
Cathode thickness, d_c (μm)	100
Height of gas flow channel (mm)	1.0
Length of the planar SOFC (mm)	20
Thickness of interconnect (mm)	0.5
Inlet velocity: U_{in} ($\text{m}\cdot\text{s}^{-1}$)	1.0
Cathode inlet gas molar ratio: O_2/N_2	0.21/0.79
Anode inlet gas molar ratio: $\text{H}_2\text{O}/\text{CH}_4$	0.667/0.333
SOFC operating potential (V)	0.8
Thermal conductivity of SOFC component ($\text{W}\cdot\text{m}^{-1}\cdot\text{K}^{-1}$)	
Anode	11.0
Electrolyte	2.7
Cathode	6.0
Interconnect	1.1

Table 2. Parameters used in calculating the effective diffusion coefficients [65]

	CO	CO ₂	H ₂	O ₂	CH ₄	N ₂	H ₂ O
σ_i	3.69	3.941	2.827	3.467	3.758	3.798	2.641
ε_i/k	91.7	195.2	59.7	106.7	148.6	71.4	809.1

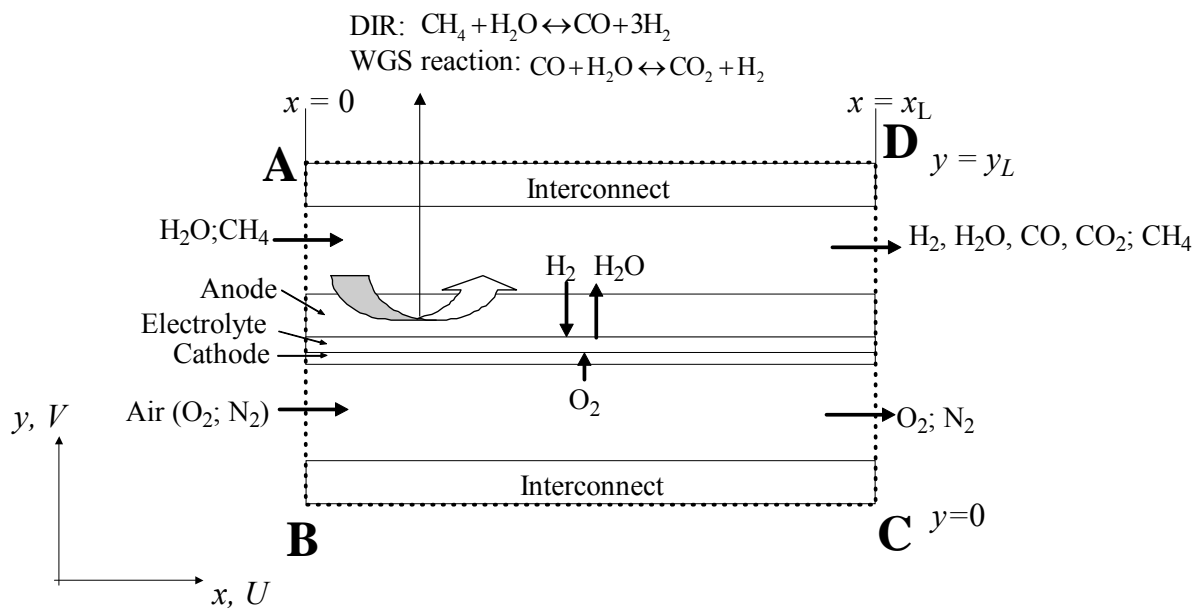
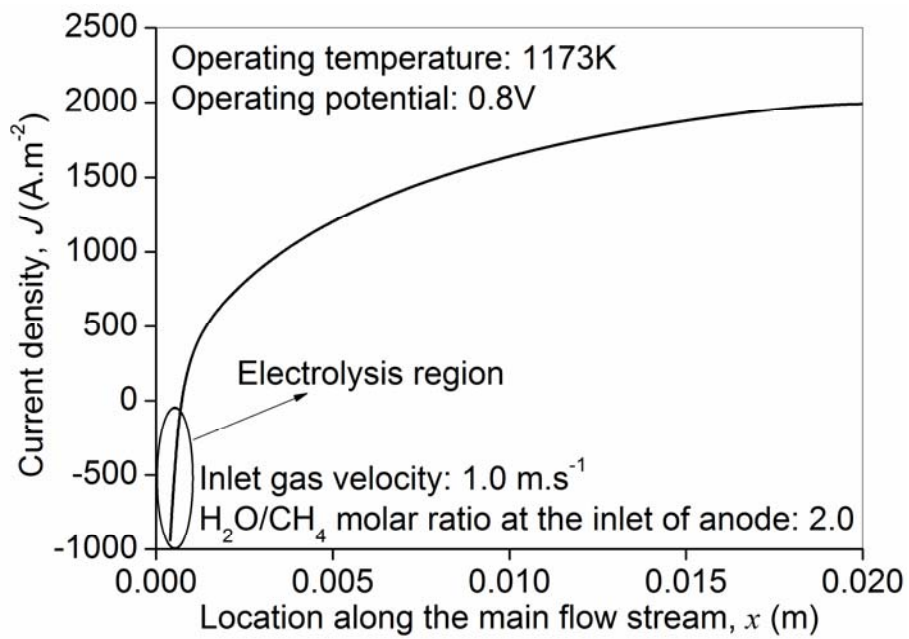
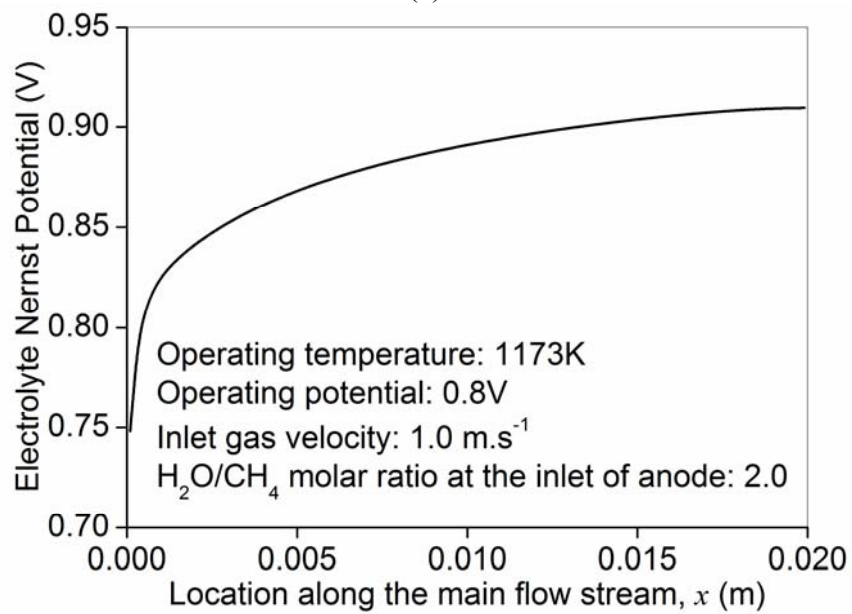


Figure 1.

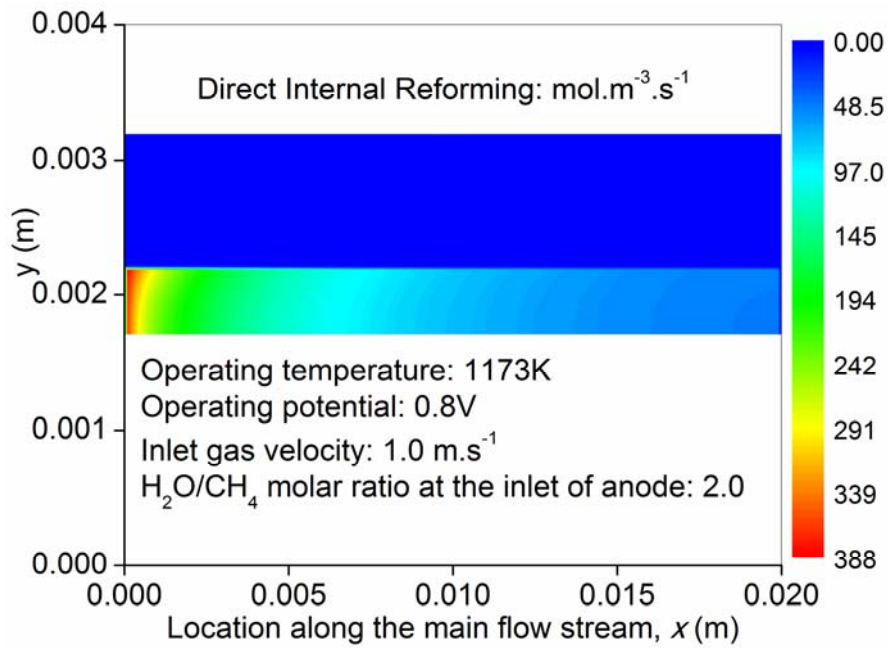


(a)

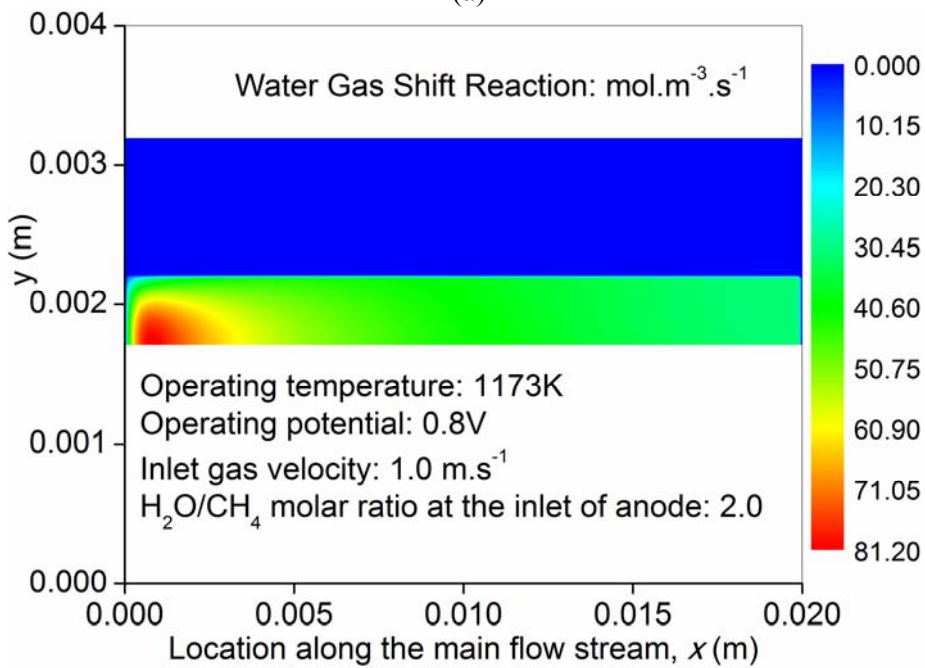


(b)

Fig. 2.

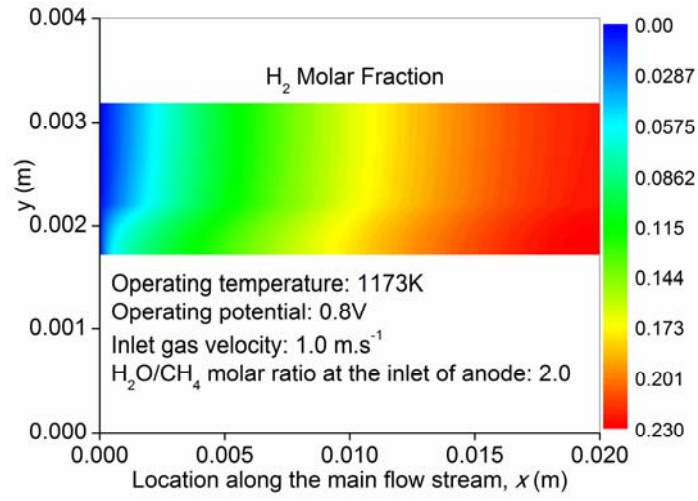


(a)

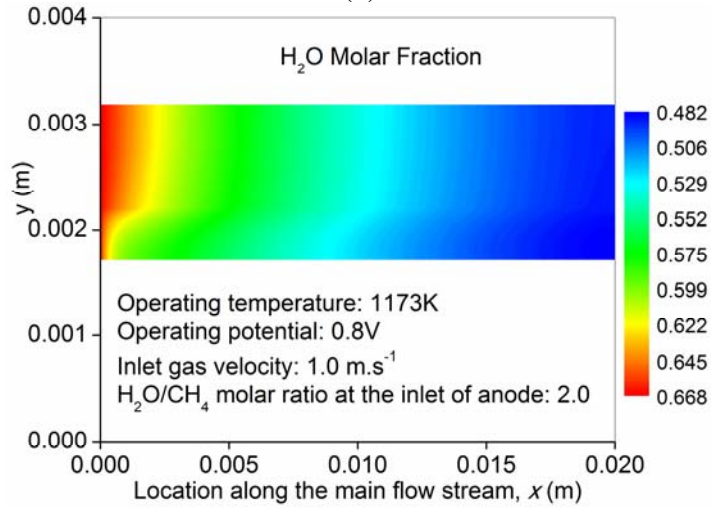


(b)

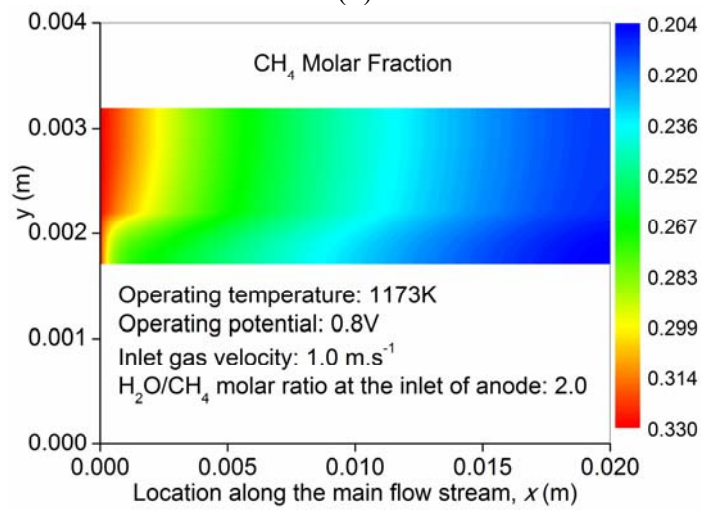
Fig. 3.



(a)



(b)



(c)

Fig. 4.

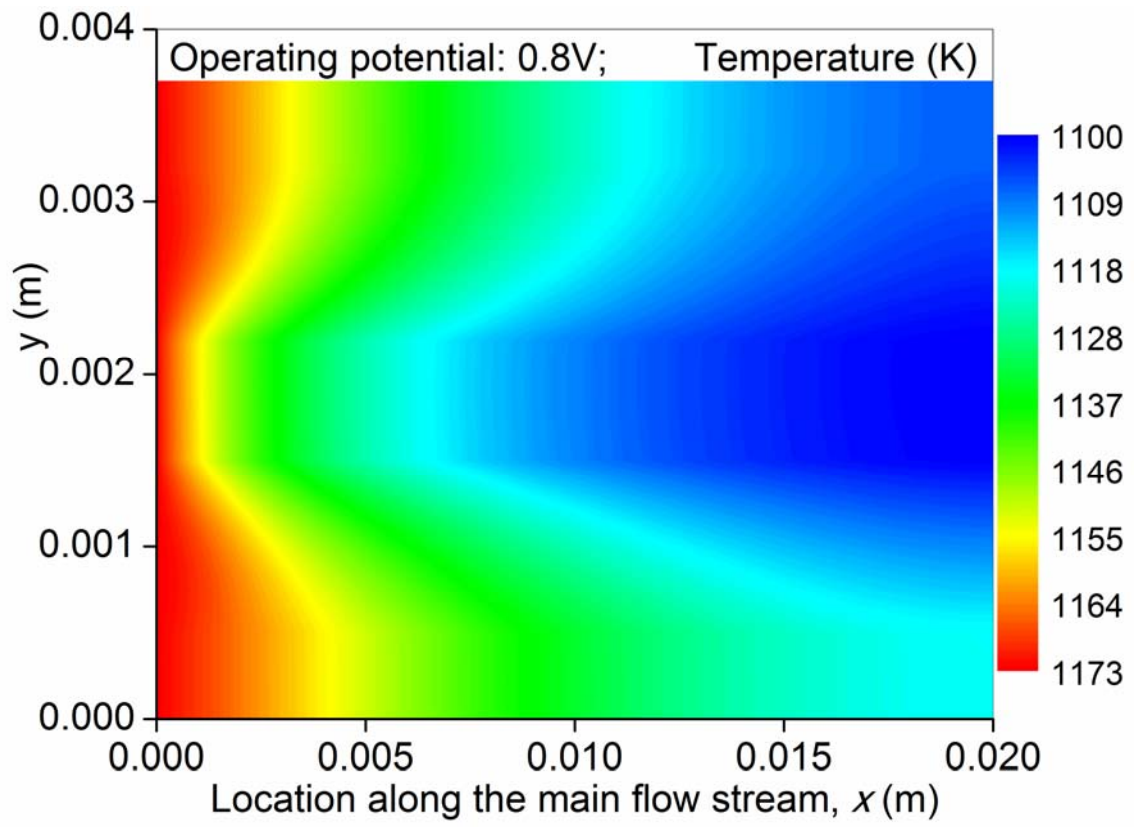
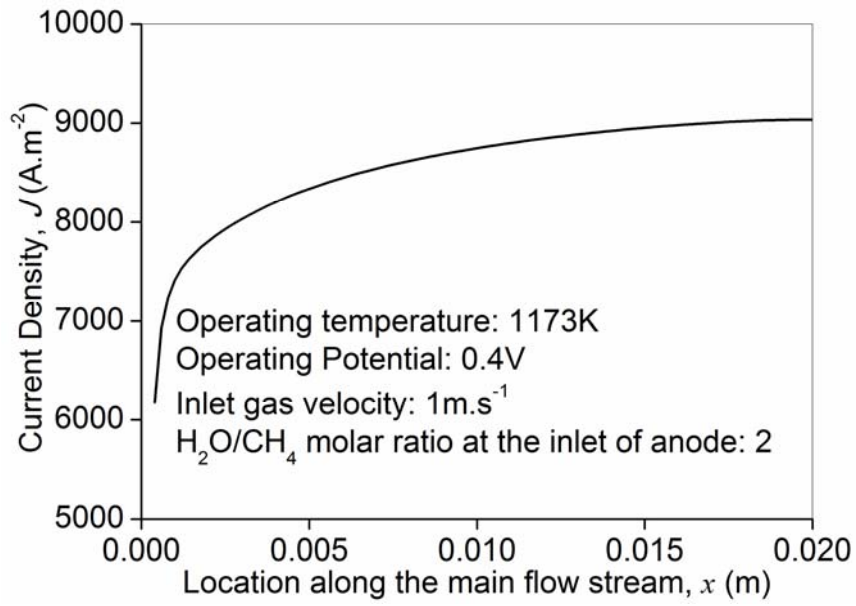
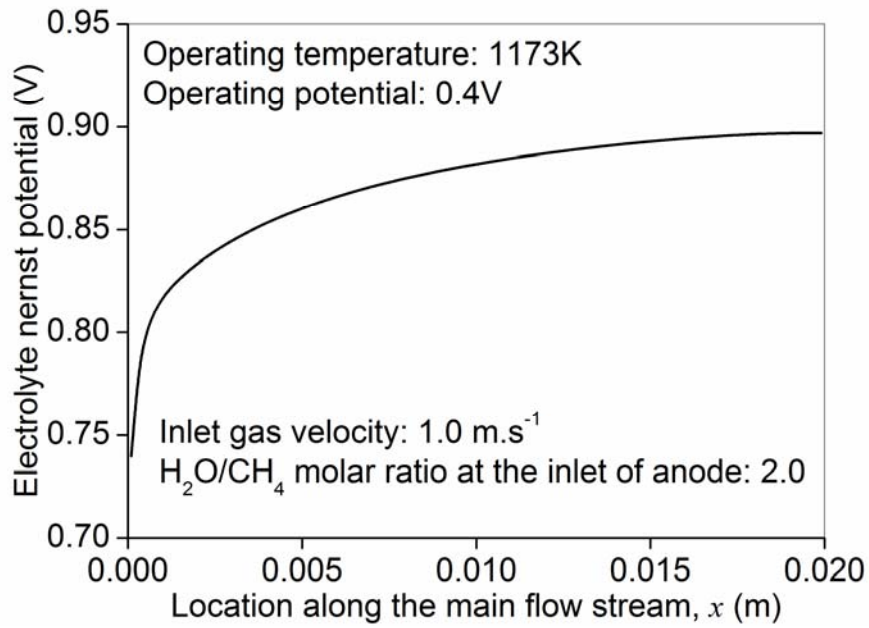


Fig. 5.



(a)



(b)

Fig. 6.

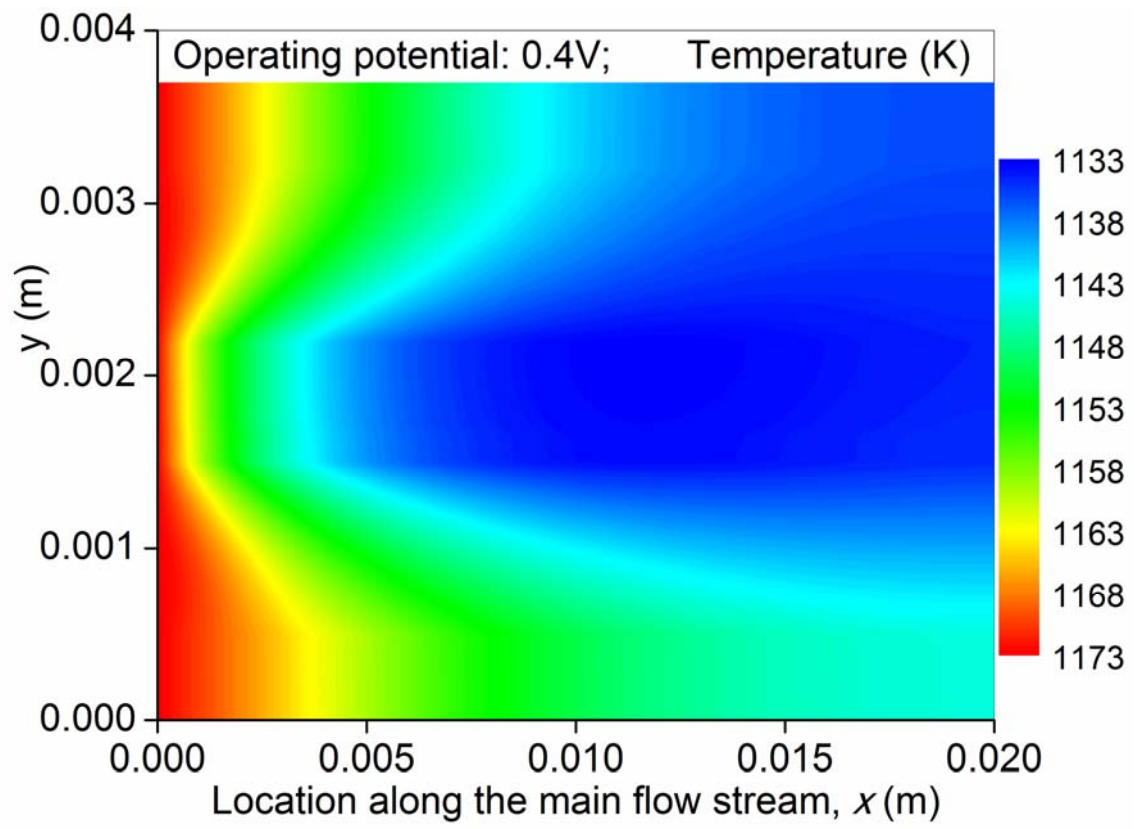
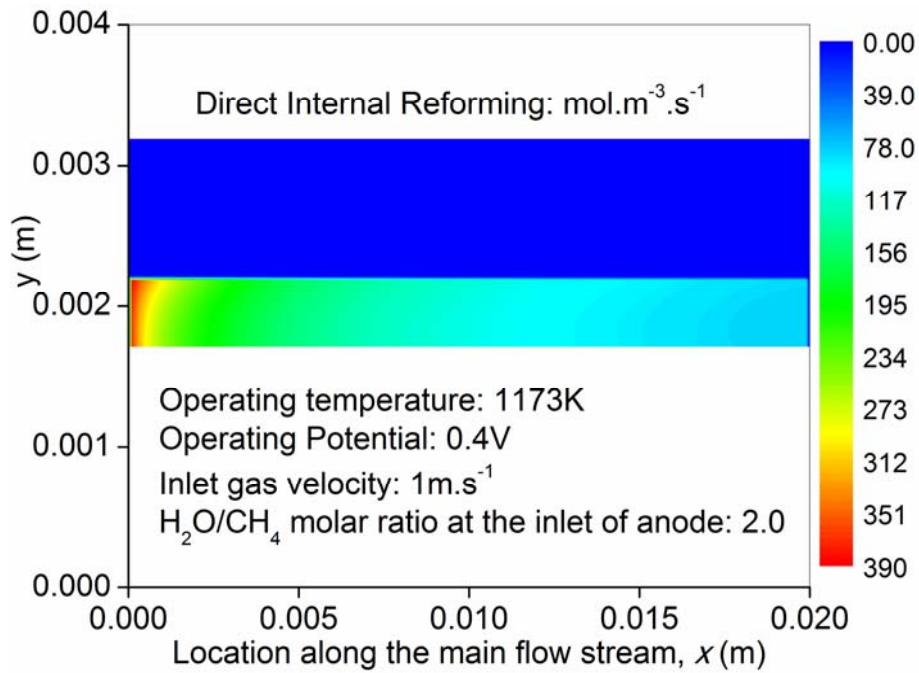
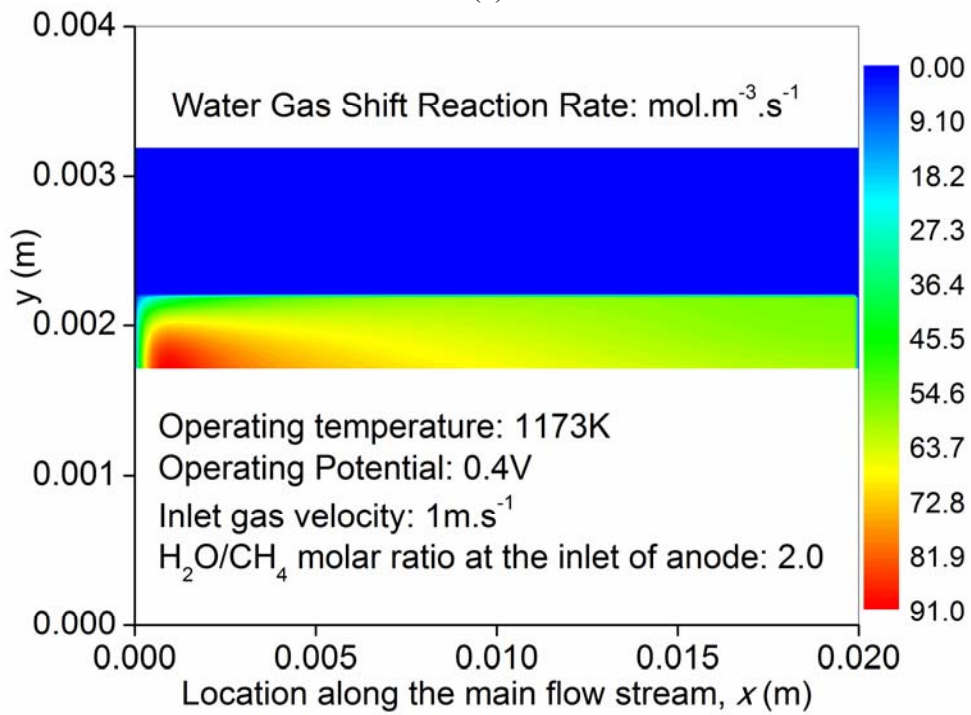


Fig. 7

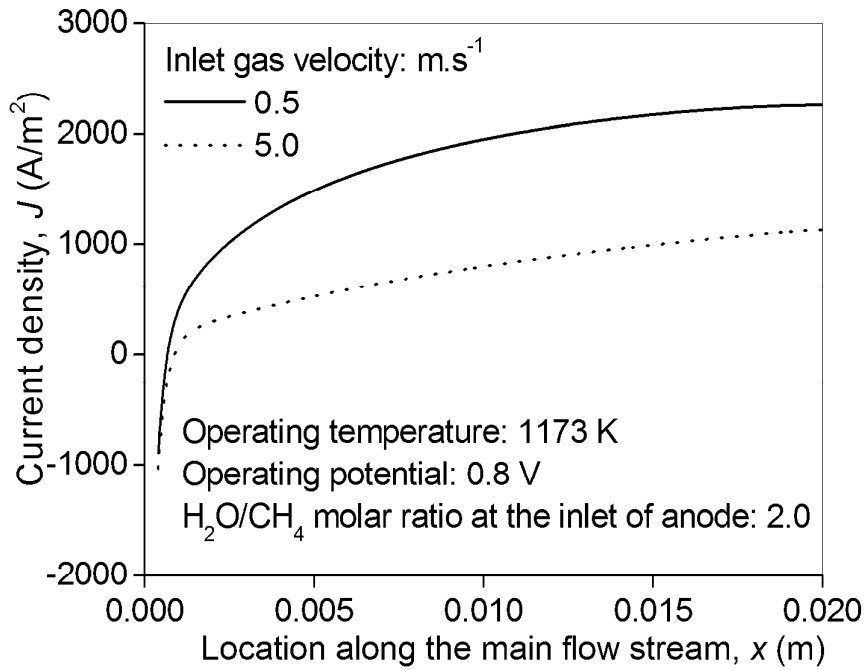


(a)

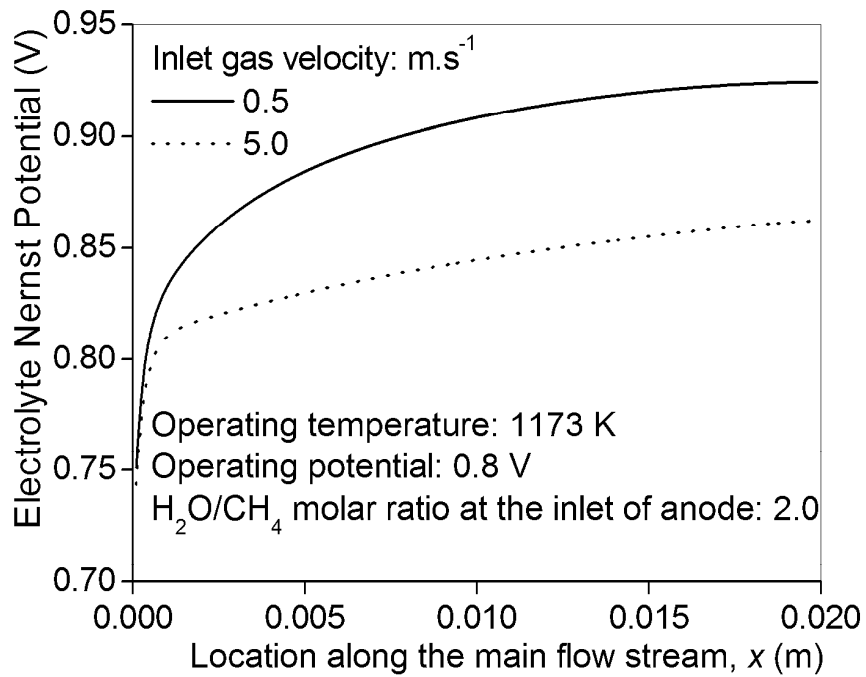


(b)

Fig. 8.



(a)



(b)

Fig. 9.

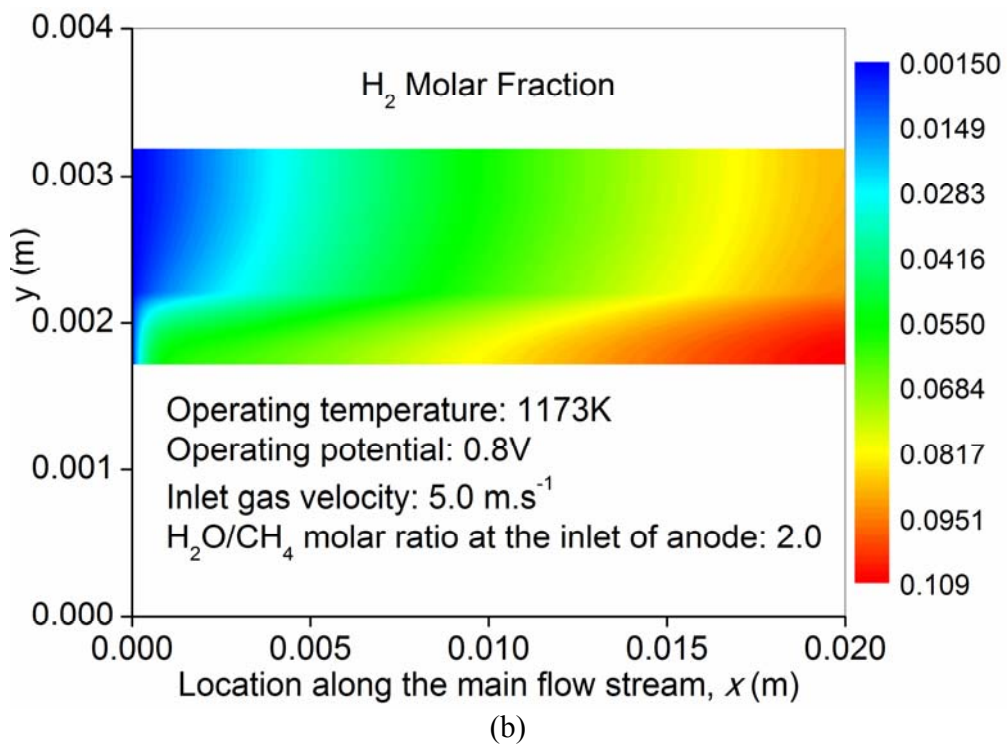
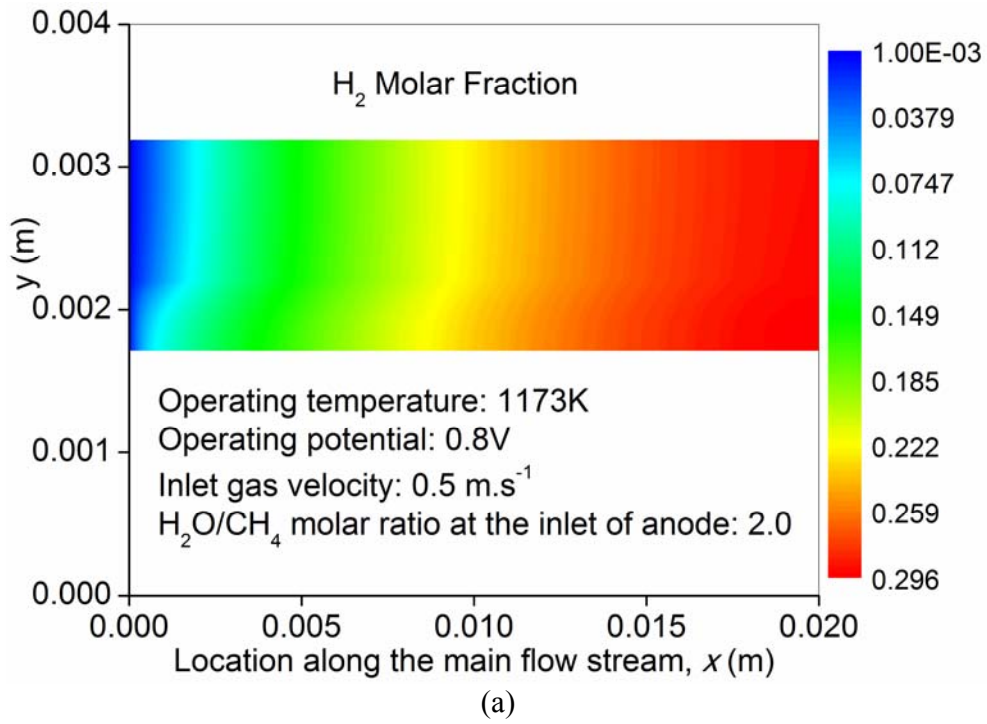
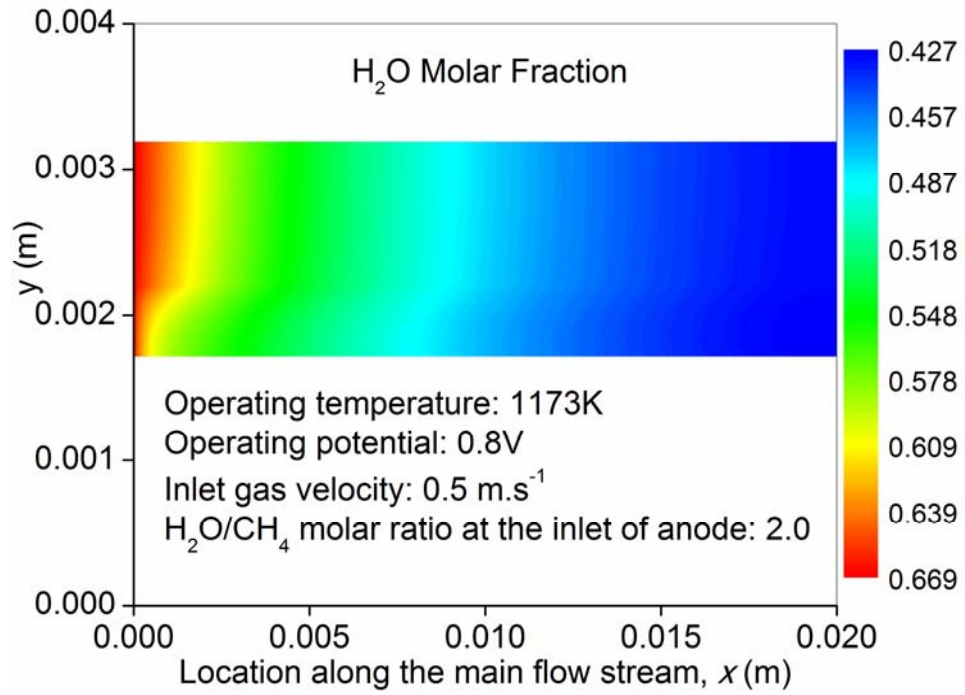
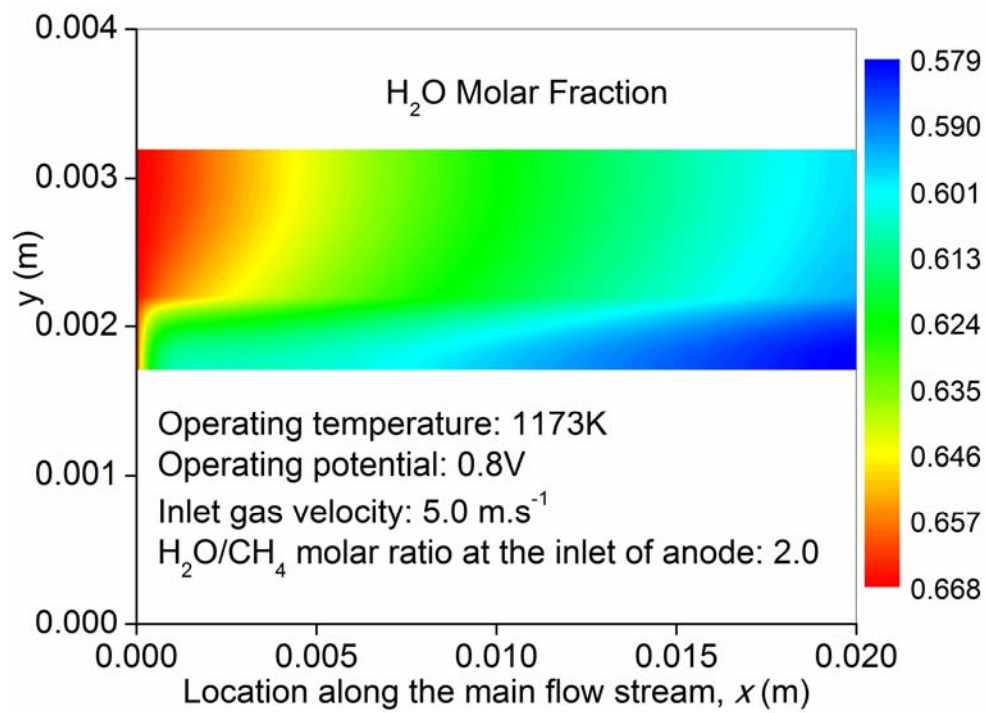


Fig. 10

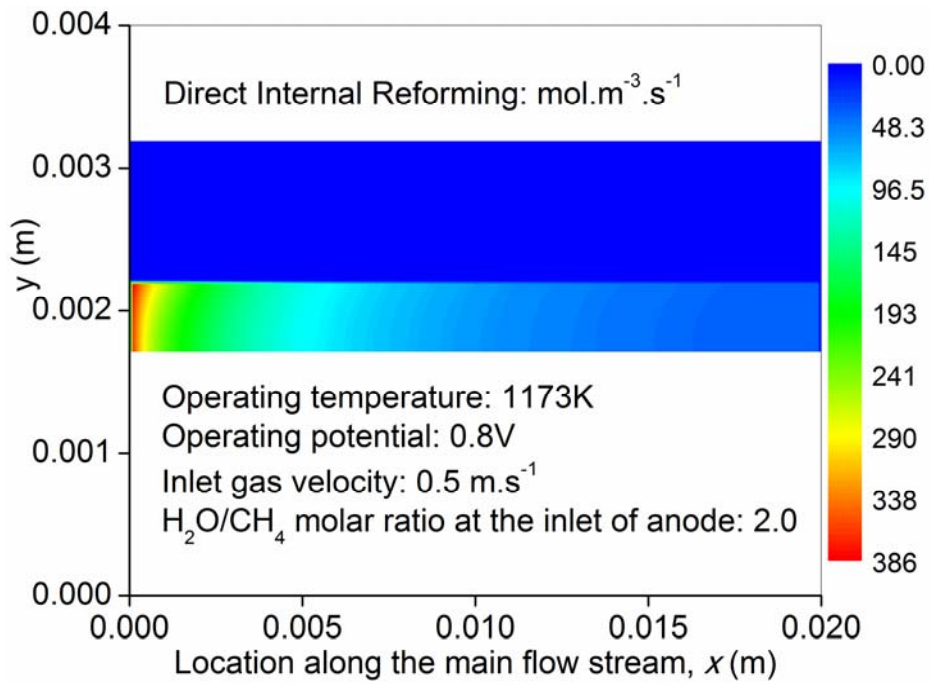


(a)

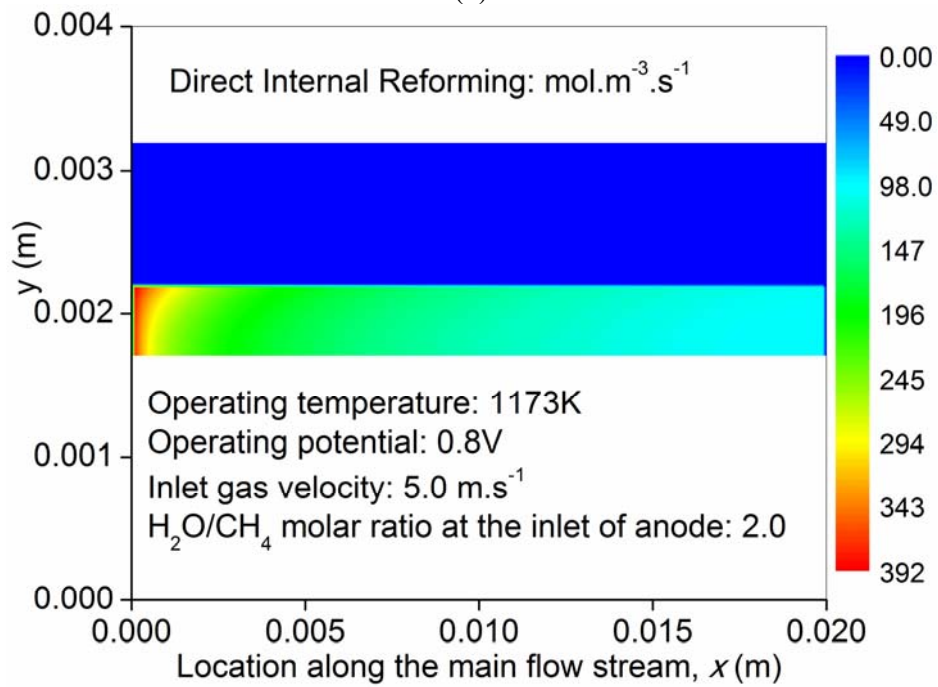


(b)

Fig. 11



(a)



(b)

Fig. 12

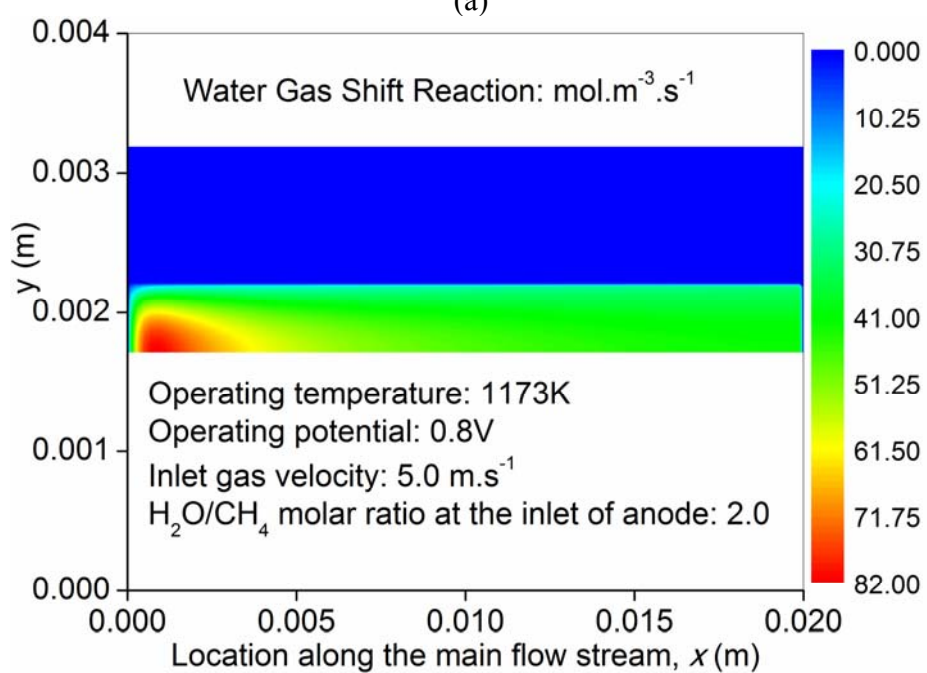
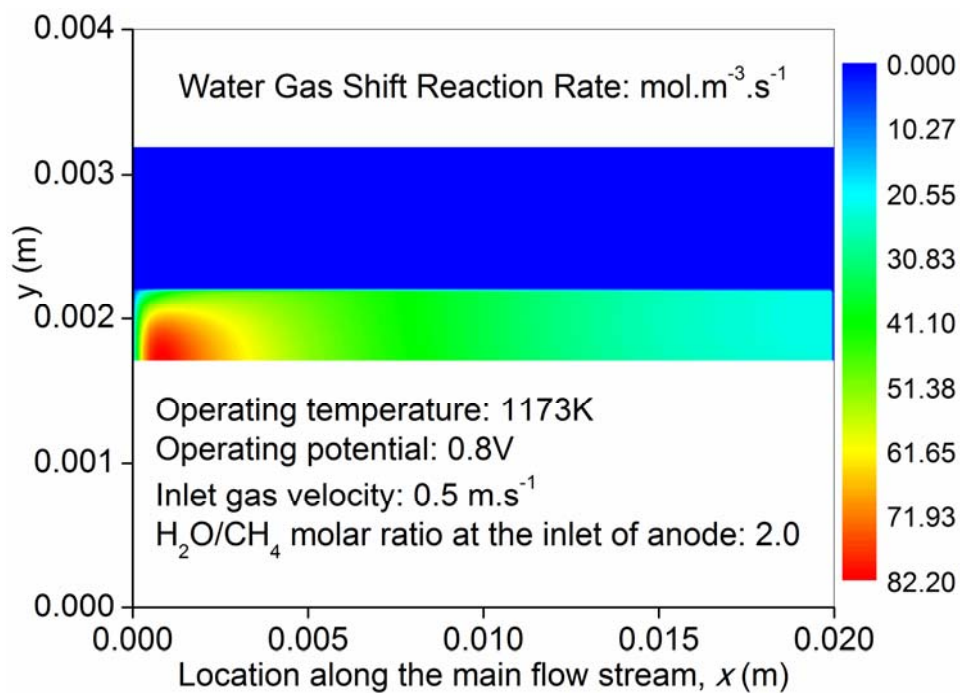


Fig. 13